Microfluidic magnetic self-assembly at liquid-liquid interfaces

Steven G. Jones,[a] Niki Abbasi,[a] Byeong-Ui Moon,[a]and Scott S. H. Tsai[ab]*

Received Xth XXXXXXXXXX 20XX, Accepted Xth XXXXXXXXX 20XX
First published on the web Xth XXXXXXXXXX 200X
DOI: 10.1039/b000000x

We present a microfluidic method that controllably self-assembles microparticles into clusters at an aqueous two-phase liquid-liquid interface. The liquid-liquid interface is formed between converging flows of aqueous dextran and polyethylene glycol, in a microfluidic cross-slot device. We control the size of the self-assembled particle clusters as they pass through the liquid-liquid interface, by systematically varying the applied magnetic field gradient, and the interfacial tension of the liquid-liquid interface. We find that upon penetration through the interface, the number of particles within a cluster increases with increasing interfacial tension, and decreasing magnetic field gradient. We also develop a scaling model of the number of particles within a cluster, and observe an inverse scaling of the number of particles within a cluster with the dimensionless magnetic Bond number. Upon cluster penetration across the liquid-liquid interface, we find magnetic Bond number regimes where the fluid coating drains away from the surface of the cluster, and where the clusters are encapsulated inside a thin film coating layer. This self-assembly technique may find application in controlling the size of microscale self-assemblies, and coating such assemblies; for example, in clustering and coating of cells for immunoisolated cell transplants.

1 Introduction

The interface formed between immiscible liquid phases has numerous applications in microfluidic devices.[1,2] Liquid-liquid interfaces are important in separation processes,[3,4] particle synthesis techniques,[5,6] and are well-known for their use in self-assembly systems.[7,8]

Recently, microfluidic technologies have facilitated the self-assembly of a variety of particle clusters. For example, spherical particle clusters can be formed in evaporating drops,[9] and Janus particles formed with droplet microfluidics can be designed to self-assemble into highly repeatable cluster geometries.[10,11]

Particles and particle clusters can also be forced through a liquid-liquid interface, to conformally coat the particles and assemblies in a thin film of one of the two immisible fluid phases.[12–14] For example, self-assembly and conformal coating of microparticle clusters has been demonstrated in a microfluidic system by magnetically pulling the microparticles across a two-phase co-flow oil-water interface.

Forcing microparticles through a liquid-liquid interface via body forces such as magnetic forces is only possible when the interface between the liquid phases has an ultra-low interfacial tension.[15] For oil-water systems, ultra-low interfacial tension is achieved with the use of surfactants.[12,15] However, surfactants have practical limitations. For example, above the critical micelle concentration (CMC), additional surfactants do not go to the interface to reduce the interfacial tension, but instead form micelles in the bulk fluid phase.[15]

A more suitable interface for particle passage may involve aqueous two-phase systems (ATPS), which are formed by dissolving two incompatible polymers in water, that phase separate above a critical dissolved polymer concentration. ATPS naturally have ultra-low interfacial tension, that can be tuned by adjusting the dissolved polymer concentration,[16] without adding any surfactants. Additionally, ATPS are all-biocompatible, so self-assembly and coating systems that use ATPS could be easily adapted for biological applications, such as cell clustering and coating.[14,17–19]

Despite recent interest in microfluidic interfacial self-assembly, there has not been a robust method that controls the self-assembly process and the final cluster size. In this manuscript, we describe a microfluidic method that controls the self-assembly of paramagnetic microparticles on a liquid-liquid interface. Specifically, we control the number of particles within a particle cluster by systematically varying the strength of the applied magnetic field gradient, and the interfacial tension of the liquid-liquid interface. We also develop a simple scaling model of the size of the self-assembled clusters, based on the magnetic form of the dimensionless Bond number. Our experimental results show a good agreement with our model.

The ATPS liquid-liquid interface in our experiments is formed in an extensional flow, between converging flows of aqueous polyethylene glycol (PEG) and dextran (DEX). Extensional flows in the microfluidic cross-slot geometry have

[a]*Ryerson University, Mechanical and Industrial Engineering, Toronto, Canada. E-mail: scott.tsai@ryerson.ca*
[b]*Keenan Research Centre, Li Ka Shing Knowledge Institute, St. Michael's Hospital, Toronto, Canada.*

been used primarily to study the dynamics of single polymer molecules,[20] bulk polymer rheology,[21,22] and the deformation of microcapsules in a flow field.[23] This type of flow can also be used as a hydrodynamic trap, due to the stagnation point formed when the Reynolds number is small,[24,25] and due to vortices formed when the Reynolds number is large.[26] In our microfluidic device, we use the extensional flow in the microchannel to reduce the speed of the microparticles as they arrive at the liquid-liquid interface.

This manuscript is organized as follows: we first report our experimental observations of the self-assembly of microparticles on the liquid-liquid interface. Then, we describe experimental results of the number of particles within the self-assemblies when they pass through the liquid-liquid interface. Here, we find that the number of particles within a cluster increases with increasing interfacial tension, and with decreasing magnetic field strength. These observations are captured in our simple scaling model. Finally, we show that, in a particular regime of the magnetic Bond number, the particles and particle clusters entrain a thin coating film of fluid as they pass through the liquid-liquid interface.

2 Experimental Methods

2.1 Chemical preparation

We prepare the ATPS by combining aqueous solutions of polyethylene glycol (PEG, Mw 35k, Sigma-Aldrich, St. Louis, MO, USA) and dextran (DEX, Mw 500k, Pharmacosmos, Holbaek, Denmark). The polymer concentration and fluid properties of the eight ATPS used in our experiments are summarized in Table 1. The preparation procedure is based on the methodology of Atefi *et al.*[16]

For each ATPS, a pair of 100 mL stock solutions of PEG and DEX is prepared, where the stock solutions consist of 5.0 - 20.0 % (w/v) PEG and 6.4 - 25.6 % (w/v) DEX, dissolved in deionized (DI) water. Each pair of PEG and DEX stock solutions is combined, vigorously mixed, and left for >24 hours to completely separate. The high-density DEX-rich phase is then separated from the low-density PEG-rich phase with syringes (BD Medical, Franklin Lakes, NJ, USA). We use a glass viscometer to measure the DEX and PEG phase viscosities, η_d and η_p, respectively, and we use the values of interfacial tension reported by Atefi *et al.*[16]

We use polystyrene-based paramagnetic microparticles that have radius $a = 5\,\mu$m (Sigma-Aldrich, St. Louis, MO, USA) in our experiments. We find that these microparticles partition to the DEX phase when they are mixed with our DEX-PEG ATPS. Therefore, in preparation for experiments, 100 µL of the stock microparticle solution (5% solid concentration) is added to 1 mL of the DEX phase, and thoroughly mixed with a vortex mixer. The particle suspension is then flash cen-

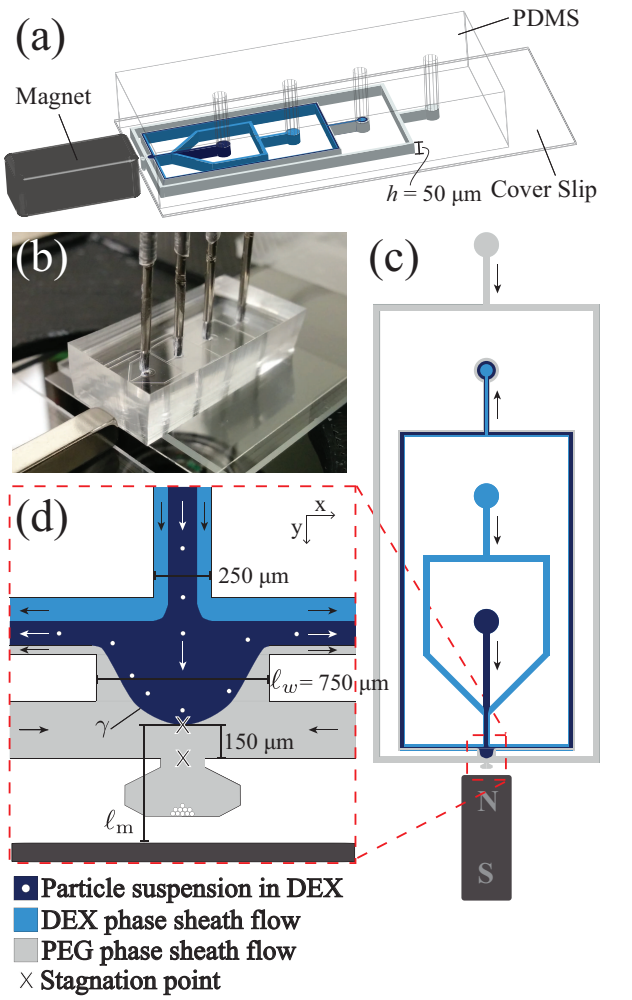

Fig. 1 (a) Schematic diagram of the microfluidic chip. A patterned layer of PDMS is plasma-bonded to a glass cover slip. A permanent magnet is placed at the edge of the microfluidic chip to provide the magnetic field. (b) Experimental set-up of the of microfluidic system with attached inlet and outlet ports. The microfluidic chip and permanent magnet are aligned on a 3D printed fixture (not shown), where the face of the magnet is centered on the cross-slot region of the microchannel. (c) Top view of the microchannel system. Paramagnetic microparticles suspended in the DEX solution are injected into the channel, and flow-focused by a DEX phase sheath flow. The total DEX phase flow converges with the PEG phase to form a stable curved liquid-liquid interface in the cross-slot chamber. Arrows indicate the direction of flow. (d) An expanded view of the cross-slot chamber shows the curved liquid-liquid interface formed from converging PEG and DEX flows. Stagnation points, shown by the symbol ×, are formed at the apex of the liquid-liquid interface, and at the throat of the cluster collection chamber. Particles that enter the cross-slot chamber at the center of the DEX-rich flow reach the apex of the liquid-liquid interface, and pass through the interface into the PEG phase collection chamber.

Table 1 Composition of the eight dextran-polyethylene glycol ATPS [b]

ATPS	PEG % (w/v)	DEX % (w/v)	η_p (mPa·s)	η_d (mPa·s)	γ (mN/m)
1	5.0	6.4	5.1	14.7	0.012
2	5.0	16.0	9.8	32.3	0.037
3	5.0	20.0	12.6	50.2	0.042
4	10.0	12.8	15.0	65.1	0.082
5	10.0	16.0	16.4	67.5	0.103
6	10.0	20.0	28.0	153.3	0.150
7	15.0	19.2	39.1	248.7	0.209
8	20.0	25.6	89.3	713.9	0.381

b ATPS number, PEG and DEX stock solution polymer weight fractions, and values of interfacial tension γ, are from Atefi *et al.* [16]

trifuged in a conical vial, and the carrier liquid is removed with a pipette. The washed microparticle pellet is then resuspended in 1 mL of the DEX phase, and loaded into a 1 mL syringe for the experiments.

2.2 Device fabrication

The microfluidic chip is fabricated with a layer of polydimethylsiloxane (PDMS, Sylgard 184, Dow Corning, Midland, MI, USA), patterned with the standard soft lithography technique. [27,28] The microchannel geometry is drawn with computer-aided design (CAD) software and printed onto a transparency sheet (25,400 dpi, CAD/ART Services Inc., Bandon, OR, USA) to form a photomask. We spin-coat SU-8 2025 negative photoresist (Microchem., Newton, MA) onto a 4-inch silicon wafer, and expose the substrate to UV light through the photomask. After the silicon wafer is developed, the PDMS channels are formed by pouring PDMS (10:1 prepolymer to curing agent) over the silicon wafer, which is then cured in an oven, to produce microchannels with height $h = 50$ μm.

The edge of the patterned PDMS layer is trimmed with a straight razor (Personna, Verona, VA, USA), to allow the placement of a permanent magnet in close proximity ($<$1 mm) to the cross-slot region of the microchannel. Inlet and outlet holes are punched into the patterned PDMS layer with a 1 mm diameter biopsy punch (Integra Miltex, Inc., Rietheim-Weilheim, Germany). The patterned PDMS layer is then permanently bonded via oxygen plasma treatment (Harrick Plasma, Ithaca, NY, USA) to a glass cover slip ($50 \times 22 \times 0.2$ mm; Thermo Fisher Scientific Inc., MA, USA) with the cross-flow region of the PDMS layer placed at the outside edge of the glass slide (see Figs. 1 (a) and (b)).

2.3 Experimental setup

Fig. 1 (c) shows a top view of the microchannels in the PDMS device. Paramagnetic microparticles suspended in the DEX phase are injected into the microfluidic device, where they are flow-focused by a DEX phase sheath flow. The flow-focused DEX phase converges with the PEG phase in the cross-slot chamber to form a stable liquid-liquid interface. The combined PEG and DEX phases then flow into symmetrical outlets in an extensional flow. Fig. 1 (d) shows a magnified schematic diagram of the microfluidic cross-slot, where particles suspended in the DEX phase flow to the liquid-liquid interface.

Under flow conditions, a cross-slot microchannel geometry produces an extensional flow field, with a stagnation point at the center of the converging flows. [21,22] In our device, stagnation points are formed at the apex of the liquid-liquid interface, and at the throat of the collection chamber in the PEG phase [24] (marked with $\times$ in Fig. 1 (d)). The width of the microchannel at the cross-slot junction also expands from 250 μm at the DEX-side of the chamber, to $\ell_w = 750$ μm at the junction. As a result of this channel geometry, the liquid-liquid interface has a curved shape, with the stagnation point located at the apex of the curved interface.

The main benefit of applying an extensional flow is that that the stagnation point—which forms on the liquid-liquid interface as a result of the extensional flow—significantly reduces the speed of the fluid at the apex of the liquid-liquid interface, and thus reduces the drag force experienced by the microparticles during the self-assembly process. Additionally, the extensional flow brings particles directly to the liquid-liquid interface, which is advantageous over previous co-flow self-assembly systems where the particles must be magnetically forced through the bulk fluid phase to reach the interface. [12,13,15] Finally, the geometry of the microchannel causes the liquid-liquid interface to be curved, which drives the self-assembly process toward the apex of the curve, and thus produces larger clusters than what has been observed in co-flow self-assembly microchannels. [12]

We use a single neodymium iron boron magnet (NdFeB, B22X0, K. J. Magnetics, Jamison, PA, USA), with magnetization $M \approx 1.05$ MA/m, which is placed in close proximity to the cross-junction of the microchannel (Fig. 1 (b)). The

magnetization direction is indicted in Fig. 1 (c). A 3D printed fixture is used to control the alignment of the microfluidic chip and the permanent magnet. As seen in Fig. 1 (b), the magnet is secured to a glass slide to allow repeatable alignment of the magnet. The magnet is positioned such that the center of the magnet face is aligned with the cross-flow region of the microchannel, to reduce the vertical and lateral components of the magnetic field gradient.

The microparticle suspension and the two aqueous phases are pumped with syringe pumps (Harvard Apparatus, Holliston, MA, USA), through polyethylene tubing (Instech Laboratories, Inc., PA, USA), to the corresponding inlets of the microfluidic device. Syringes are interfaced with the tubing via blunt needle syringe tips (Fishman Corporation, MA, USA). The syringe pump that controls the particle suspension flow rate is positioned vertically above the microfluidic chip. This setup reduces variations in the particle flux into the microfluidic device from particles sedimenting in the tubing. Additionally, the microparticle suspension is remixed just prior to each experiment to ensure a homogeneous mixture. Within the typical timescale of a set of experiments (∼30 min.), we do not observe a significant variation in the particle flux coming into the microchannel.

The flow rates of the microparticle suspension and the DEX phase sheath flow are each set to 2 µL/min, for a total DEX phase flow rate $Q_d = 4$ µL/min. The PEG phase flow rate is initially set to $Q_p = 2$ µL/min. Due to the different viscosity ratios of the PEG and DEX phases for different ATPS compositions, small adjustments in the PEG flow rate (Q_p = 1.8 - 4.4 µL/min) are required to maintain the 150 µm distance between the apex of the liquid-liquid interface and the PEG phase channel wall (see Fig 1 (d))).

Most experimental images are captured using an inverted microscope (IX71, Olympus Corp., Tokyo, Japan) with a 20x objective, and an attached high speed camera (Miro M110, Vision Research, Wayne, NJ, USA) operating at a frame rate of 100 fps, and an exposure time of 1,000 µs. High resolution images are taken with a 50x objective, at a frame rate of 200 fps, and an exposure time of 500 µs. ImageJ is used for image processing.[29]

3 Results and Discussion

3.1 Self-assembly at the DEX-PEG liquid-liquid interface

We observe that microparticles that reach the apex of the liquid-liquid interface self-assemble into clusters due to the local magnetic field gradient provided by the permanent magnet. If the self-assembled particle cluster is sufficiently large, it will pass through the liquid-liquid interface into the PEG phase. Fig. 2 (a) shows an experimental image of the cross-slot chamber during the extensional flow and self-assembly process. Here, particles enter the chamber from the upper DEX inlet, and flow towards the liquid-liquid interface.

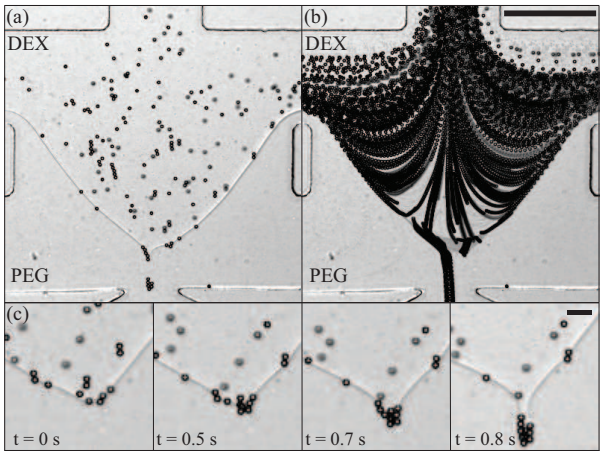

Fig. 2 Experimental image of (a) the cross-flow chamber, with an applied magnetic field, during the magnetic cluster self-assembly process. (b) Experimental image of the particle trajectories during self-assembly. Scale bar indicates 250 µm. (c) A close-up time-series view of a microparticle cluster forming on the liquid-liquid interface, where the cluster with particle number $N = 9$ is formed on an interface with interfacial tension $\gamma = 0.103$ mN/m. Scale bar indicates 50 µm.

Fig. 2 (b) shows the trajectories of microparticles as they flow through the cross-slot chamber in the presence of a magnetic field. This figure illustrates the motion of the microparticles in the chamber during the self-assembly process, and the image is compiled by stacking multiple frames from a ∼ 1 s video. Microparticles in the center of the DEX phase flow directly to the apex of the liquid-liquid interface, where the particles are able to self-assemble into a cluster. Particles that are farther from the center of the channel when they enter the cross-slot chamber are deflected away from the centerline by the bulk fluid flow, but are often still able to reach the liquid-liquid interface. Some of the particles that reach the interface will move towards the apex of the liquid-liquid interface and will self-assemble. The particles that reach the interface farther away from the stagnation point will eventually flow with the bulk fluid to one of the symmetrical side outlets.

Fig. 2 (c) shows time series images of a particle cluster as it self-assembles on the liquid-liquid interface, and passes through to the PEG phase. In this case, the microparticles assemble into a cluster with particle number $N = 9$, and then pass through the liquid-liquid interface into the PEG phase. A representative video of interfacial self-assembly is provided as Supplementary Movie 1.

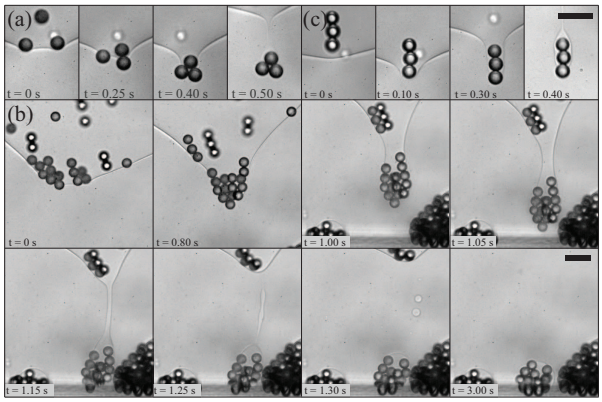

Fig. 3 Experimental images of microparticle clusters passing through the liquid-liquid interface. We observe interfacial self-assembly, where (a) individual microparticles and (b) particle chains assemble at the liquid-liquid interface, and magnetic self-assembly, where (c) magnetic particle chains pass through the liquid-liquid interface without further interactions with other particles and chains at the interface. In (a) and (c), the liquid-liquid interfacial tension $\gamma = 0.103$ mN/m. In (b), the interfacial tension $\gamma = 0.209$ mN/m. Scale bars indicate 25 µm.

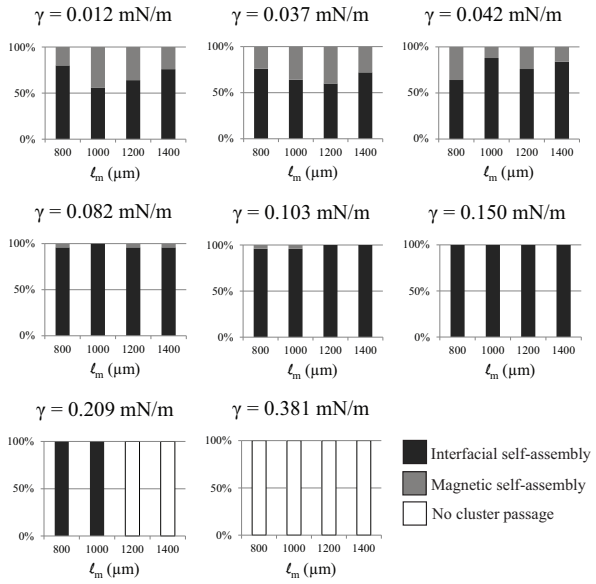

Fig. 4 Stacked bar graphs showing the percentage of each self-assembly type, versus magnet distance ℓ_m. Interfacial self-assembly and magnetic self-assembly are indicated by black and gray bars, respectively, and white bars show instances where none of the self-assembled clusters were able to pass through the interface. The results from each set of magnet distance ℓ_m and interfacial tension γ are from the first 25 clusters that pass through the liquid-liquid interface in each experimental video.

3.2 Different types of self-assembled clusters

Due to the combination of interfacial effects from the presence of the liquid-liquid interface, magnetic effects from the magnetic field, and hydrodynamic forces from the extensional flow field, we observe two types of particle self-assembly. In interfacial self-assembly, individual magnetic particles and particle chains self-assemble at the liquid-liquid interface (see for example Figs. 3 (a) and (b), respectively). In magnetic self-assembly, magnetic particle chains form upstream of the liquid-liquid interface, and pass through the liquid-liquid interface without further interaction with other particles at the interface (see for example Fig. 3 (c)).

In our experiments, we observe that in the region of influence of the magnetic field, paramagnetic particles in close proximity (approximately one particle radius) to each other are able to align into chains, due to magnetic dipole-dipole interactions. We observe this behavior most frequently with two individual particles aligning into a doublet, but particle chains with a larger number of particles also form. We observe that the formation of particle chains frequently occurs as particles enter the cross-slot chamber, due to the increased strength of the magnetic field as the particles flow closer to the magnet.

In systems that have higher interfacial tension γ, smaller particle chains, such as doublets, are not able to pass through the interface. Instead, these chains self-assemble at the liquid-liquid interface with other particles, to form larger clusters (see Fig. 3 (b)). If the liquid-liquid interfacial tension γ is sufficiently low, microparticle chains formed upstream to the interface are able to pass directly though the interface without any other interactions at the interface (see Fig. 3 (c)).

Fig. 4 shows a comparison of the percentages of interfacial self-assembly and magnetic self-assembly, for each combination of interfacial tension γ and magnet distance ℓ_m. Here, the percentages are calculated by observing the first 25 clusters that pass through the ATPS interface. We find that most clusters are formed via interfacial self-assembly, which implies that the liquid-liquid interface plays a critical role in determining the size of the clusters. Most of the magnetic particle chains that form upstream of the liquid-liquid interface also self-assemble with other particles at the liquid-liquid interface. Since interfacial assembly appears to be the dominant mechanism for self-assembly in our technique, we focus only on interfacial self-assembly in the remaining data analyses in this manuscript.

3.3 Controlling the size of self-assembled clusters

We control the number of particles N within individual clusters, by systematically varying the location of the magnet ℓ_m (Fig. 1 (d)), and by adjusting the liquid-liquid interfacial tension γ. Fig. 5 shows a plot of the cluster particle number N

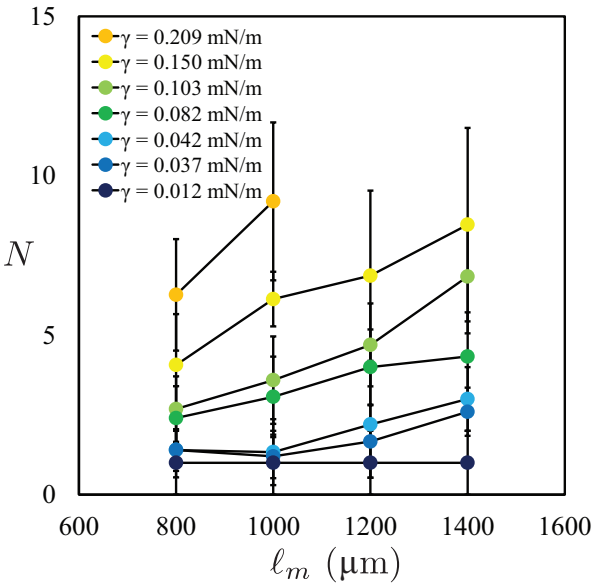

Fig. 5 A plot of the cluster particle number N versus magnet position ℓ_m, where ℓ_m is the distance between the magnet face and the apex of the liquid-liquid interface. The interfacial tension γ of the liquid-liquid interface is varied by adjusting the dissolved polymer concentration of the ATPS (summarized in Table 1). We observe that particle number N increases with magnet distance ℓ_m, and also grows with interfacial tension γ. Error bars represent one standard deviation.

versus the magnet distance ℓ_m. Each point represents the average of the first 15 samples in an experimental video.

We observe that as we increase the magnet distance ℓ_m, which reduces the strength of the magnetic field, a greater number of particles N is required to overcome the interfacial tension energy barrier, and pass through the interface. We also modify the interfacial tension γ of the liquid-liquid interface, by adjusting the ATPS polymer concentration (see Table 1), to see how this affects the self-assembly process. We observe an approximately monotonic increase of the cluster particle number N with increasing magnet distance ℓ_m, and with increasing interfacial tension γ (Fig. 5).

At the interface, it is the competition of magnetic forcing and interfacial restoring energy that determines whether a particle or cluster is able to pass through the interface. Therefore, the force balance at equilibrium in the direction normal to the ATPS interface at the apex reads,

$$F_m \approx F_\gamma \tag{1}$$

where on N particles, the magnetic force,[30]

$$F_m = 4\pi N a^3 \mu_o \frac{\chi}{\chi+3}\frac{\partial H^2}{\partial y}. \tag{2}$$

Here, μ_o = 1.257 $\times 10^{-6}$ m kg s^{-2} A^{-2} is the permeability of free space, $\chi \approx O(10^{-3})$ is the magnetic susceptibility of our magnetic particles,[15] and $\boldsymbol{H}$ is the magnetic field. A plot of the magnetic field, $\boldsymbol{H}$, is shown in Supplementary Information Fig. S1. The interfacial tension restoring force has the magnitude $F_\gamma \approx 2\pi\gamma\ell_c$, where the particle cluster characteristic length is defined by $\ell_c^3 \approx Na^3$, or $\ell_c \approx aN^{1/3}$.[31]

Non-dimensionalizing via $\boldsymbol{H} = M\hat{\boldsymbol{H}}$, $y = \ell_m\hat{y}$, and recognizing that since $\chi << 1$, so $\frac{\chi}{\chi+3} \rightarrow O(\chi)$, we rearrange (1) to obtain,

$$2N^{2/3}Bo_m\frac{\partial \hat{H}^2}{\partial \hat{y}} - 1 = 0, \tag{3}$$

where the magnetic Bond number,

$$Bo_m = \frac{a^2M^2\chi\mu_o}{\ell_m\gamma}. \tag{4}$$

With our choice of non-dimensionalization, $\frac{\partial \hat{H}^2}{\partial \hat{y}} = O(1)$ (assuming that the magnetic field $\boldsymbol{H}$ varies by approximately the amount M, across a distance ℓ_m). Therefore,

$$N = \kappa Bo_m^{-3/2}, \tag{5}$$

where κ is a constant prefactor that we can determine experimentally.

Fig. 6 shows a log-log plot of the cluster particle number N versus the magnetic Bond number, Bo_m. We observe that

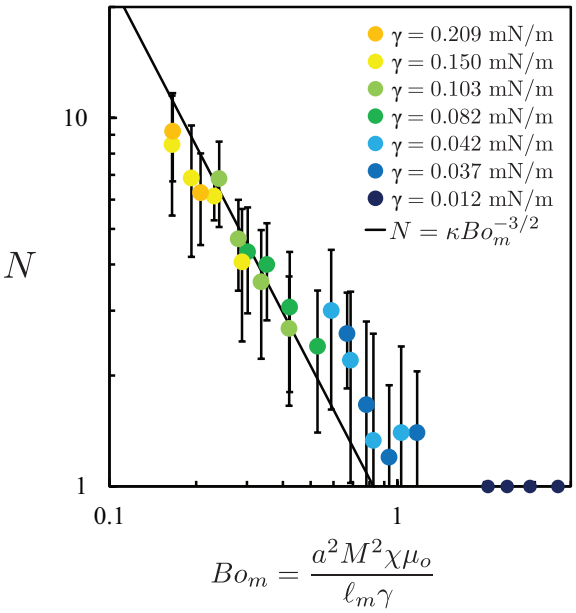

Fig. 6 Log-log plot of the cluster particle number N, against the dimensionless magnetic Bond number, Bo_m. We observe that the particle number scales as $N = \kappa Bo_m^{-3/2}$, where $\kappa \approx 0.75$. Error bars represent one standard deviation.

the number of particles N within a cluster decreases with increasing magnetic Bond number, and the experimental results show a good agreement with our model, $N = \kappa Bo_m^{-3/2}$, where the constant prefactor $\kappa \approx 0.75$. Interestingly, this is the same power law that we observed previously, for millimeter length-scale sphere clusters formed by stacking spheres on an oil-water interface in a large glass tank.[31]

At higher values of the magnetic Bond number, we note that the model predicts a smaller cluster size N than what we observe experimentally. We attribute this to the tendency of particles, that are in the region of influence of a strong magnetic field—corresponding to a large value of the magnetic Bond number, Bo_m—to align into chains via strong dipole-dipole interactions. The chain cluster geometry leads to the characteristic length $\ell_c \to a$, and (1) reduces to $N \propto Bo_m^{-1}$. We note that our data tends to deviate further from our model when interfacial tension γ is low, which also corresponds to lower fluid viscosities η_d and η_p (see Table 1). The lower viscosities may allow the particles to reorient into chains more readily, due to a lower drag force, which also contributes to final cluster sizes that may be larger than the predicted critical size N.

3.4 Coating and non-coating of particle clusters

Fig. 7 (a) shows images from an experiment with a small magnetic Bond number ($Bo_m \approx 0.3$), where a paramagnetic particle flowing into the cross-flow chamber approaches the liquid-liquid interface. The DEX fluid film between the particle and the liquid-liquid interface completely drains away at $t \approx 0.2$ s, where the three-phase contact line is formed and the particle "snaps-in" to the ATPS interface. The particle subsequently detaches from the interface at $t \approx 1.15$ s, and passes into the PEG phase. This type of particle passage is analogous to the drainage regime in the classical fluid mechanics literature,[32,33] and the "snap-in" behavior had previously been observed by Sinha *et al.*[4] in a co-laminar flow geometry. The film drainage process is gradual, so we also observe instances where particles become adsorbed onto the liquid-liquid interface, remain on the interface, and are washed into one of the side channels with the moving fluid.

Fig. 7 (b) shows that, in the larger magnetic Bond number regime (in this case $Bo_m \approx 3$), the magnetic force overcomes the restoring force from the liquid-liquid interface. The particle passes from the DEX phase, into the PEG phase, without becoming adsorbed onto the liquid-liquid interface. Particles that pass through the liquid-liquid interface in this manner entrain a thin film of the DEX phase as they pass through the interface. The entrained DEX phase forms an interfacial tail behind the particle as the particle moves through the PEG phase. This type of particle passage is analogous to the tailing regime in the classical fluid mechanics literature.[32,33]

Particle clusters that pass through the liquid-liquid inter-

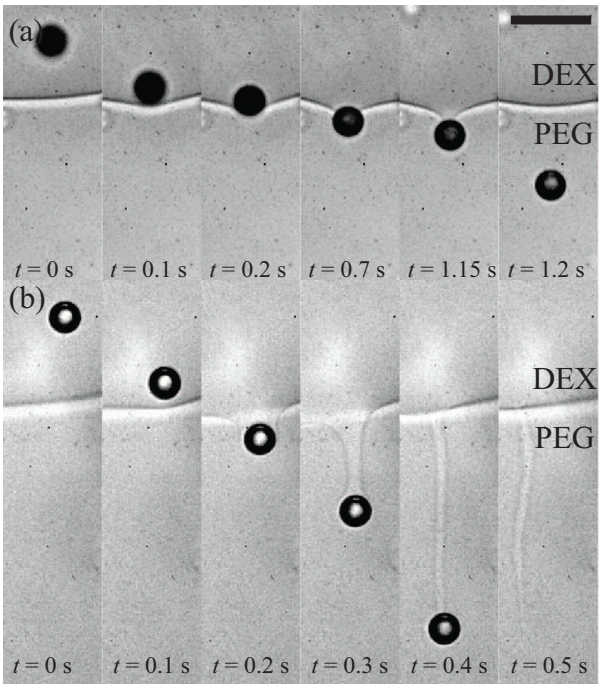

Fig. 7 (a) Experimental images of a single microparticle passing through the liquid-liquid interface in the drainage regime, where the DEX fluid film completely drains away, before the particle is able to pass through the interface. Here, the three-phase contact line forms at $t \approx 0.2$ s, when the particle adsorbs onto the interface. The particle detaches from the interface after $t \approx 1.15$ s, then passes into the PEG phase. The interfacial tension $\gamma = 0.150$ mN/m. (b) A single particle passing through the interface in the tailing regime. As the particle approaches the liquid-liquid interface, the interface deforms rapidly, and the particle is able to pass through the interface without forming a three-phase contact line. As the particle continues into the PEG phase, it entrains some of the DEX phase in an interfacial tail. Here, the interfacial tension $\gamma = 0.012$ mN/m. Scale bar indicates 25 μm.

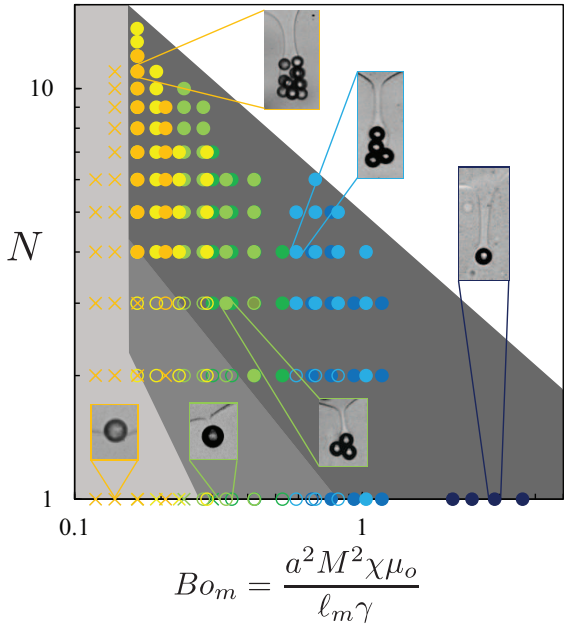

Fig. 8 Fluid entrainment regime map for particles and clusters. Here, solid circles represent particle and/or cluster passage in the tailing regime, open circles indicate the drainage regime, and crosses indicate that particles do not cross the liquid-liquid interface (no passage). Marker colors correspond to the interfacial tensions γ, in Figs. 5 and 6. We observe that when the magnetic Bond number Bo_m is large, most particle clusters pass through the interface in the tailing regime, which is characterized by the entrainment of a thin coating film of the DEX phase with the particle cluster. As the magnetic Bond number Bo_m is reduced, particles pass though the interface in the drainage regime, which is characterized by the complete drainage of the DEX phase liquid film from the particle surface. Here, the particles are able to pass through the interface, but are not encapsulated in a coating layer of the DEX phase. When the magnetic Bond number Bo_m is very small, the particles are not able to pass through the liquid-liquid interface. Gray shaded areas indicate the approximate boundaries between the tailing, drainage, and no passage regimes.

face in a high Bond number regime also entrain a thin coating film of the DEX phase as they pass into the PEG phase. Fig. 8 shows a regime map of fluid entrainment by particle clusters. We plot each self-assembly experiment on a log-log plot of the particle number N versus the magnetic Bond number Bo_m. Solid circles represent the tailing regime, where particles and/or clusters pass through the interface and entrain a thin film of the DEX phase. Open circles represent the drainage regime, where particles and/or clusters pass through the interface, but all of the DEX phase drains away prior to the particles passing through the interface. Crosses represent instances where particles and clusters are not able to pass through the interface. The gray shaded areas indicate the approximate boundaries between the tailing, drainage, and no passage regimes (dark gray, medium gray, and light gray, respectively).

For single particles, if the magnetic Bond number Bo_m is greater than unity (i.e. magnetic forces dominate interfacial restoration), microparticles cross the liquid-liquid interface without forming a three-phase contact line, and pass into the PEG phase while retaining a coating layer of DEX. As the particles continue into the PEG phase, the interfacial tail behind the particle thins and eventually ruptures. As we reduce the magnetic Bond number Bo_m to approximately unity, particles that reach the interface are adsorbed onto the interface, and form the three-phase contact line. These particles are able to detach from the interface to pass into the PEG phase, but do not become coated with a film of the DEX phase.

We make a similar observation for particle clusters. When the magnetic Bond number Bo_m is large, particle clusters pass through the liquid-liquid interface in the tailing regime, and entrain a thin film of the DEX phase. At lower values of the magnetic Bond number Bo_m, the clusters approach the liquid-liquid interface in the drainage regime, and the DEX fluid layer completely drains away before the clusters pass through the interface. However, we observe that the transition between the tailing and drainage regimes occurs at a lower value of the magnetic Bond number Bo_m, for particle clusters, in comparison to individual particles.

4 Conclusions

In this manuscript, we describe a microfluidic technique that self-assembles paramagnetic microparticles into clusters on a liquid-liquid interface. We show that, the number of particles within a cluster can be tuned by adjusting the interfacial tension γ of the liquid-liquid interface, and the strength of the magnetic field. We find that, the number of particles N within a cluster, scales with a power law of the magnetic Bond number, such that $N \propto Bo_m^{-3/2}$.

We also observe that in the large magnetic Bond number regime, particle clusters that pass through the liquid-liquid interface entrain a thin film of the DEX fluid phase. Therefore, this system may be applicable to forming coated clusters of other paramagnetic materials, and may be particularly well suited to generating coated cell clusters with magnetically tagged cells–for example, to immunoisolate the cells for cell transplantation operations.[34–36] The ability to control the size of the coated cluster, in an all-biocompatible ATPS environment, will be desirable in these biomedical applications.

In the present setup, coated clusters will coalesce upon contact in the collection reservoir. Therefore, achieving useful cell clustering and coating will require the implementation of a polymerization scheme that solidifies the coating film. Additionally, the efficiency of this particle cluster formation and coating technique can be improved with the addition of more serial flow focusing junctions, so that particles enter the cross-flow chamber in approximately a straight line, and all reach the apex (stagnation point) of the liquid-liquid interface. We anticipate that these two improvements will help move this microfluidic technique closer to cellular immunoisolation applications.

5 Acknowledgments

S. S. H. Tsai (grant no. 435514-2013) thanks the Natural Sciences and Engineering Research Council (NSERC) of Canada for supporting this project through the Discovery grant program. N. Abbasi acknowledges Ryerson University's Faculty of Engineering and Architectural Science (FEAS) for the Dean's Research Fund for Undergraduate Research Experience (DRF-URE). S. G. Jones thanks Ryerson University and the Ontario Ministry of Training, Colleges, and Universities (MTCU) for the Queen Elizabeth II Graduate Scholarship in Science and Technology (QEII-GSST). Finally, the authors acknowledge association with the Institute for Biomedical Engineering and Science Technology (iBEST)—a partnership between Ryerson University and St. Michael's Hospital.

References

1 C.-X. Zhao, *Advanced Drug Delivery Reviews*, 2013, **65**, 1420–1446.
2 M. D. Tarn, M. J. Lopez-Martinez and N. Pamme, *Analytical and Bioanalytical Chemistry*, 2014, **406**, 139–161.
3 J. R. SooHoo and G. M. Walker, *Biomedical Microdevices*, 2009, **11**, 323–329.
4 A. Sinha, A. K. Mollah, S. Hardt and R. Ganguly, *Soft Matter*, 2013, **9**, 5438–5447.
5 D. Dendukuri and P. S. Doyle, *Advanced Materials*, 2009, **21**, 4071–4086.
6 H. C. Shum, A. R. Abate, D. Lee, A. R. Studart, B. Wang, C.-H. Chen, J. Thiele, R. K. Shah, A. Krummel and D. A. Weitz, *Macromolecular Rapid Communications*, 2010, **31**, 108–118.
7 R. McGorty, J. Fung, D. Kaz and V. N. Manoharan, *Materials Today*, 2010, **13**, 34–42.

8 Y. Lin, H. Skaff, T. Emrick, A. Dinsmore and T. Russell, *Science*, 2003, **299**, 226–229.

9 G.-R. Yi, T. Thorsen, V. N. Manoharan, M.-J. Hwang, S.-J. Jeon, D. J. Pine, S. R. Quake and S.-M. Yang, *Advanced Materials*, 2003, **15**, 1300–1304.

10 Z. Nie, W. Li, M. Seo, S. Xu and E. Kumacheva, *Journal of the American Chemical Society*, 2006, **128**, 9408–9412.

11 T. M. Ruhland, A. H. Groschel, N. Ballard, T. S. Skelhon, A. Walther, A. H. Muller and S. A. Bon, *Langmuir*, 2013, **29**, 1388–1394.

12 S. S. H. Tsai, J. S. Wexler, J. Wan and H. A. Stone, *Applies Physics Letters*, 2011, **99**, 153509.

13 B.-U. Moon, N. Hakimi, D. K. Hwang and S. S. Tsai, *Biomicrofluidics*, 2014, **8**, 052103.

14 A. Khademhosseini, M. H. May and M. V. Sefton, *Tissue Engineering*, 2005, **11**, 1797–1806.

15 S. S. Tsai, J. S. Wexler, J. Wan and H. A. Stone, *Lab on a Chip*, 2013, **13**, 119–125.

16 E. Atefi, J. A. Mann Jr and H. Tavana, *Langmuir*, 2014, **30**, 9691–9699.

17 G. Orive, R. M. Hernández, A. R. Gascón, R. Calafiore, T. M. Chang, P. De Vos, G. Hortelano, D. Hunkeler, I. Lacík, A. J. Shapiro *et al.*, *Nature Medicine*, 2003, **9**, 104–107.

18 K. Vijayakumar, S. Gulati, J. B. Edel *et al.*, *Chemical Science*, 2010, **1**, 447–452.

19 C. Moraes, A. B. Simon, A. J. Putnam and S. Takayama, *Biomaterials*, 2013, **34**, 9623–9631.

20 T. T. Perkins, D. E. Smith and S. Chu, *Science*, 1997, **276**, 2016–2021.

21 F. J. Galindo-Rosales, M. Alves and M. Oliveira, *Microfluidics and Nanofluidics*, 2013, **14**, 1–19.

22 S. Haward, A. Jaishankar, M. Oliveira, M. Alves and G. McKinley, *Biomicrofluidics*, 2013, **7**, 044108.

23 C. de Loubens, J. Deschamps, M. Georgelin, A. Charrier, F. Edwards-Levy and M. Leonetti, *Soft Matter*, 2014, **10**, 4561–4568.

24 J. Soulages, M. Oliveira, P. Sousa, M. Alves and G. McKinley, *Journal of Non-Newtonian Fluid Mechanics*, 2009, **163**, 9–24.

25 M. Tanyeri, E. M. Johnson-Chavarria and C. M. Schroeder, *Applied Physics Letters*, 2010, **96**, 224101.

26 D. Vigolo, S. Radl and H. A. Stone, *Proceedings of the National Academy of Sciences*, 2014, **111**, 4770–4775.

27 Y. Xia and G. M. Whitesides, *Annual Review of Materials Science*, 1998, **28**, 153–184.

28 B.-U. Moon, S. G. Jones, D. K. Hwang and S. S. Tsai, *Lab on a Chip*, 2015.

29 M. D. Abràmoff, P. J. Magalhães and S. J. Ram, *Biophotonics International*, 2004, **11**, 36–42.

30 S. S. Tsai, I. M. Griffiths and H. A. Stone, *Lab on a Chip*, 2011, **11**, 2577–2582.

31 S. G. Jones, N. Abbasi, A. Ahuja, V. Truong and S. S. Tsai, *Physics of Fluids*, 2015, **27**, 072102.

32 A. Geller, S. Lee and L. Leal, *Journal of Fluid Mechanics*, 1986, **169**, 27–69.

33 J. De Folter, V. De Villeneuve, D. Aarts and H. Lekkerkerker, *New Journal of Physics*, 2010, **12**, 023013.

34 G. Orive, R. M. Hernández, A. R. Gascón, R. Calafiore, T. M. S. Chang, P. de Vos, G. Hortelano, D. Hunkeler, I. Lacık and J. L. Pedraz, *Trends in Biotechnology*, 2004, **22**, 87–92.

35 R. H. Li, *Advanced Drug Delivery Reviews*, 1998, **33**, 87–109.

36 L. M. Weber, J. He, B. Bradley, K. Haskins and K. S. Anseth, *Acta Biomaterialia*, 2006, **2**, 1–8.